



Elongation enhances encounter rates between phytoplankton in turbulence

José-Agustín Arguedas-Leiva^{a,1}, Jonasz Słomka^{b,1}, Cristian C. Lalescu^c, Roman Stocker^b, and Michael Wilczek^{a,d,2}

Edited by David Weitz, Harvard University, Cambridge, MA; received February 22, 2022; accepted June 13, 2022

Phytoplankton come in a stunning variety of shapes but elongated morphologies dominate—typically 50% of species have aspect ratio above 5, and bloom-forming species often form chains whose aspect ratios can exceed 100. How elongation affects encounter rates between phytoplankton in turbulence has remained unknown, yet encounters control the formation of marine snow in the ocean. Here, we present simulations of encounters among elongated phytoplankton in turbulence, showing that encounter rates between neutrally buoyant elongated cells are up to 10-fold higher than for spherical cells and even higher when cells sink. Consequently, we predict that elongation can significantly speed up the formation of marine snow compared to spherical cells. This unexpectedly large effect of morphology in driving encounter rates among plankton provides a potential mechanistic explanation for the rapid clearance of many phytoplankton blooms.

encounter rates | turbulence | cell elongation | marine snow | phytoplankton blooms

Microscopic photosynthetic marine phytoplankton cells are responsible for nearly half of the global carbon fixation (1), a key biogeochemical process that fuels ocean primary production (2). While phytoplankton come in a variety of shapes (3), combined data from different aquatic habitats indicate that elongated morphologies dominate, with 50% of cells having aspect ratio greater than 5 (4). The aspect ratio of the most elongated unicellular phytoplankton (e.g., *Ulnaria*, *Rhizosolenia*) approaches 100 (3), whereas bloom-forming species, such as *Trichodesmium*, often form chains of cells that can have even higher aspect ratios (5, 6). Cell shape is recognized as a key trait determining the fitness of phytoplankton (3) because it affects nutrient uptake (7), growth rate (8), survival upon grazing by zooplankton (9), swimming direction (10), and light harvesting (11). By contrast, the impact of elongation on encounters between individual phytoplankton has only recently started to be explored (12, 13), and we still lack an understanding of how interaction between environmental determinants, such as turbulence (7, 14, 15), and biological determinants, such as cell size, elongation, and density (7, 13–15), controls encounters. Yet, physical encounters between individual phytoplankton exert a fundamental control on a broad range of processes in plankton ecology and ocean biogeochemistry. Encounters determine the formation of marine snow, which fuels the “biological pump,” the vertical export of carbon to the deep ocean that represents one of the climatically most important carbon fluxes in the ocean (14, 16–18). Encounters may also influence the composition of marine snow particles (19) by overrepresenting species that encounter frequently, as well as the rate of phytoplankton colony formation, such as the formation of mats or tufts and puffs by the highly elongated *Rhizosolenia* (20) or *Trichodesmium* (21), important players in the nitrogen and carbon cycles (22) (Fig. 1A).

Here, we present results from direct numerical simulations and scaling arguments to quantify encounter rates between thin elongated cells or chains of cells, accounting for the effects of turbulence and sinking (Fig. 1), focusing on the parameter regime characteristic of elongated phytoplankton experiencing turbulence levels typical of the ocean surface layer. We find that, for neutrally buoyant cells, elongation enhances encounter rates by 20% for cells of aspect ratio 5, 2-fold for aspect ratio 20, 7-fold for aspect ratio 100, and 10-fold for even higher aspect ratios. If cells sink or rise, such as most cells upon a bloom demise or cells that actively regulate buoyancy using gas vacuoles and carbohydrate ballasting (23, 24), respectively, we find that the combined effect of turbulence and sinking further enhances encounter rates. Based on these results, we predict that elongation can significantly accelerate the formation of marine snow compared to spherical cells. These findings provide a potential mechanistic explanation for the rapid clearance of blooms, for the frequent occurrence of highly elongated species in marine snow particles, and for the propensity of elongated species to form colonies.

To quantify the role of elongation on the encounter rates between phytoplankton cells, we conducted an extensive series of numerical simulations of millions of cells, neglecting

Significance

Encounters between phytoplankton cells are among the key microphysical processes that control global biogeochemical cycles in the ocean, e.g., through the formation of marine snow. Current models of marine snow formation that account for turbulence in the oceans represent cells as spheres, yet phytoplankton cells are often highly elongated with typical aspect ratios of five and greater. Here, we combine simulations and theory to comprehensively quantify encounter rates between elongated phytoplankton in turbulence. Remarkably, we show that encounter rates between the most elongated cells are up to 10-fold higher than between spherical cells. We predict that these enhanced encounter rates accelerate marine snow formation and thus offer a mechanistic explanation for the rapid clearance of phytoplankton blooms.

Author contributions: J.S., R.S., and M.W. designed research; J.-A.A.-L. performed numerical simulations with support from C.C.L.; J.-A.A.-L., J.S., C.C.L., and M.W. analyzed the simulation results; J.S. led the theoretical modeling; J.S. and R.S. studied the ecological consequences; and J.-A.A.-L., J.S., R.S., and M.W. wrote the paper.

The authors declare no competing interest.

This article is a PNAS Direct Submission.

Copyright © 2022 the Author(s). Published by PNAS. This article is distributed under [Creative Commons Attribution-NonCommercial-NoDerivatives License 4.0 \(CC BY-NC-ND\)](https://creativecommons.org/licenses/by-nc-nd/4.0/).

¹J.-A.A.-L. and J.S. contributed equally to this work.

²To whom correspondence may be addressed. Email: michael.wilczek@uni-bayreuth.de.

This article contains supporting information online at <https://www.pnas.org/lookup/suppl/doi:10.1073/pnas.2203191119/-DCSupplemental>.

Published August 2, 2022.

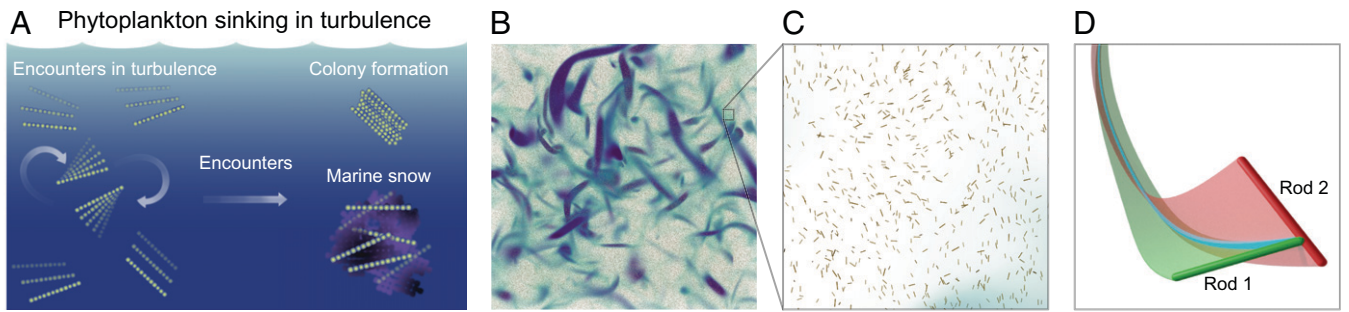


Fig. 1. (A) Encounters between phytoplankton, whose cells or chains of cells are often highly elongated, drive key ecological processes in the ocean, such as marine snow aggregation and likely colony formation. (B and C) As a model for this process, we here present results from direct numerical simulations of millions of identical rods encountering each other due to the combined effects of turbulence and sinking (Movie S1). The volume rendering shows intense vorticity structures visualizing locally swirling regions in the flow. (D) Trajectories of two encountering rods. Green and red shadings visualize the swept areas, and blue indicates the rods' overlap used to detect encounters.

inertial effects (15), across different environmental and cellular parameters (Fig. 1 B and C, Movie S1, and Materials and Methods). From the simulations, we quantified encounter rates by counting geometrical intersections between cells, which we modeled as rods (Fig. 1D and Materials and Methods). To understand the dependency of the encounter rate on environmental and cellular parameters, we computed the encounter kernel Γ . Γ represents the volume that a pair of encountering cells sweep relative to each other per unit time and is a key quantity widely used to characterize encounter rates in both physics and ecology (7, 13, 25–27).

Focusing first on neutrally buoyant cells, we found that elongated cells encounter each other more frequently than equal-volume spherical cells irrespective of the cell length or intensity of turbulence (Fig. 2 A and B). From our simulations, we computed the encounter kernel $\Gamma_{\text{rods}}^{\text{n.b.}}$ for elongated, neutrally buoyant cells (length l , aspect ratio λ) and compared it with the classic encounter kernel Γ_{ST} for neutrally buoyant spheres due to Saffman and Turner (25),

$$\Gamma_{\text{ST}} = 1.3 (2r)^3 \sqrt{\varepsilon/\nu}, \quad [1]$$

where ν is the fluid's kinematic viscosity, ε is the energy dissipation rate characterizing the turbulence intensity, and r is the radius of the spheres, which we set to match the spheres' volumes with that of elongated cells. Computing the ratio $\Gamma_{\text{rods}}^{\text{n.b.}}/\Gamma_{\text{ST}}$ for different cell lengths and aspect ratios revealed that elongation always enhanced encounter rates (Fig. 2A). This enhancement was to a good approximation independent of the cell length, which prompted us to generalize the Saffman and Turner kernel to elongated cells ("rods") by including the dependence on aspect ratio through a multiplicative factor $C(\lambda)$, as

$$\begin{aligned} \Gamma_{\text{rods}}^{\text{n.b.}} &= 1.3 l^3 \sqrt{\varepsilon/\nu} C(\lambda), \quad \text{with} \\ C(\lambda) &= -0.472\lambda^{-3} + 1.388\lambda^{-2} \\ &\quad + 0.0841\lambda^{-1} + 9.13 \times 10^{-5}. \end{aligned} \quad [2]$$

$C(\lambda)$ is a function of the cell's aspect ratio only, obtained by a fit to the simulation results (for $l = 1$ mm) and requiring that $C(1) = 1$ (Fig. 2A and SI Appendix). Thus, Eq. 2 generalizes the classic Saffman and Turner kernel to elongated cells ($\lambda > 1$) and reduces to Eq. 1 for spheres ($\lambda = 1$), as expected. To confirm the functional form of the new kernel $\Gamma_{\text{rods}}^{\text{n.b.}}$, which can be motivated by scaling arguments (SI Appendix), we considered two representative elongated cells ($l = 1$ mm, $\lambda = 100$ and $l = 80$ μm , $\lambda = 20$), varied the turbulence intensity in the simulations, and found good agreement between the resulting kernel and that predicted by Eq. 2 (Fig. 2B).

For neutrally buoyant phytoplankton, we predict from Eq. 2 that elongation increases the encounter rate by 20% for cells of aspect ratio 5, such as cells of the genera *Navicula* or *Leptocylinndrus* (3); 2-fold for aspect ratio 20, such as *Rhizosolenia*, *Nitzschia* (3), or chains of *Skeletonema* (28, 29); 7-fold for cells of aspect ratio 100, such as the most elongated cells of *Rhizosolenia* and *Ulnaria* (3); and 10-fold for the most elongated chains of *Trichodesmium* with aspect ratios above 100 (5, 6) (Fig. 2A). With this understanding of how elongation affects encounters of neutrally buoyant cells in turbulence, we next studied the encounters of elongated cells that sink in turbulence.

Cells in turbulence that also sink or rise ("buoyant cells") encounter each other even more frequently than neutrally buoyant cells. Since many phytoplankton species are denser than seawater and sink, for example following a bloom (28), or can actively modulate their buoyancy (23), we considered cells with a density offset $\Delta\rho$ compared to the ambient water. For elongated cells, a density offset induces sinking with orientation-dependent velocity (Materials and Methods). Focusing on highly elongated cells ($\lambda = 100$), we performed simulations to quantify their encounter kernel Γ_{rods} for a broad range of environmentally relevant values of their density offset and the turbulence intensity (Fig. 2C). The simulations revealed two distinct regimes: a turbulence-dominated regime for small values of $\Delta\rho$ and large values of ε (horizontal contours in Fig. 2C), in which sinking has a negligible impact on Γ_{rods} , and a sinking-dominated regime for large $\Delta\rho$ and small values of ε (vertical contours in Fig. 2C) in which sinking starts to dominate over turbulence, eventually increasing the encounter rates in proportion to the density offset.

The self-similar shape of the contour lines in Fig. 2C results from a universal scaling for the dependence of Γ_{rods} on density offset and turbulence intensity. We hypothesized that the general encounter kernel is the sum of the two kernels representing the limits of neutrally buoyant cells in turbulence and of cells sinking in a quiescent fluid; i.e.,

$$\Gamma_{\text{rods}} = \Gamma_{\text{rods}}^{\text{n.b.}} + \Gamma_{\text{rods}}^{\text{quiescent}}, \quad [3]$$

where $\Gamma_{\text{rods}}^{\text{n.b.}}$ is given by Eq. 2 and, from previous work, $\Gamma_{\text{rods}}^{\text{quiescent}} = l\beta_1(\lambda)\Delta\rho V_{\text{rod}}g/(16\lambda\mu)$, where V_{rod} is the cells' volume, μ is the fluid's dynamic viscosity, g is the gravitational acceleration, and $\beta_1(\lambda)$ is a geometrical parameter given by Eq. 12b (13). The ansatz in Eq. 3 then yields

$$\Gamma_{\text{rods}}/\Gamma_{\text{rods}}^{\text{n.b.}} = 1 + \Lambda(\lambda)u_{\text{sink}}/u_{\text{turb}}, \quad [4]$$

where $\Lambda(\lambda) = \pi/[2.6\lambda C(\lambda)]$ is a geometrical factor that depends only on the aspect ratio, and $u_{\text{sink}} = \Delta\rho V_{\text{rod}}g\beta_1(\lambda)/(8\pi\mu l)$ and $u_{\text{turb}} = l\sqrt{\varepsilon/\nu}$ are estimates of the typical relative velocities

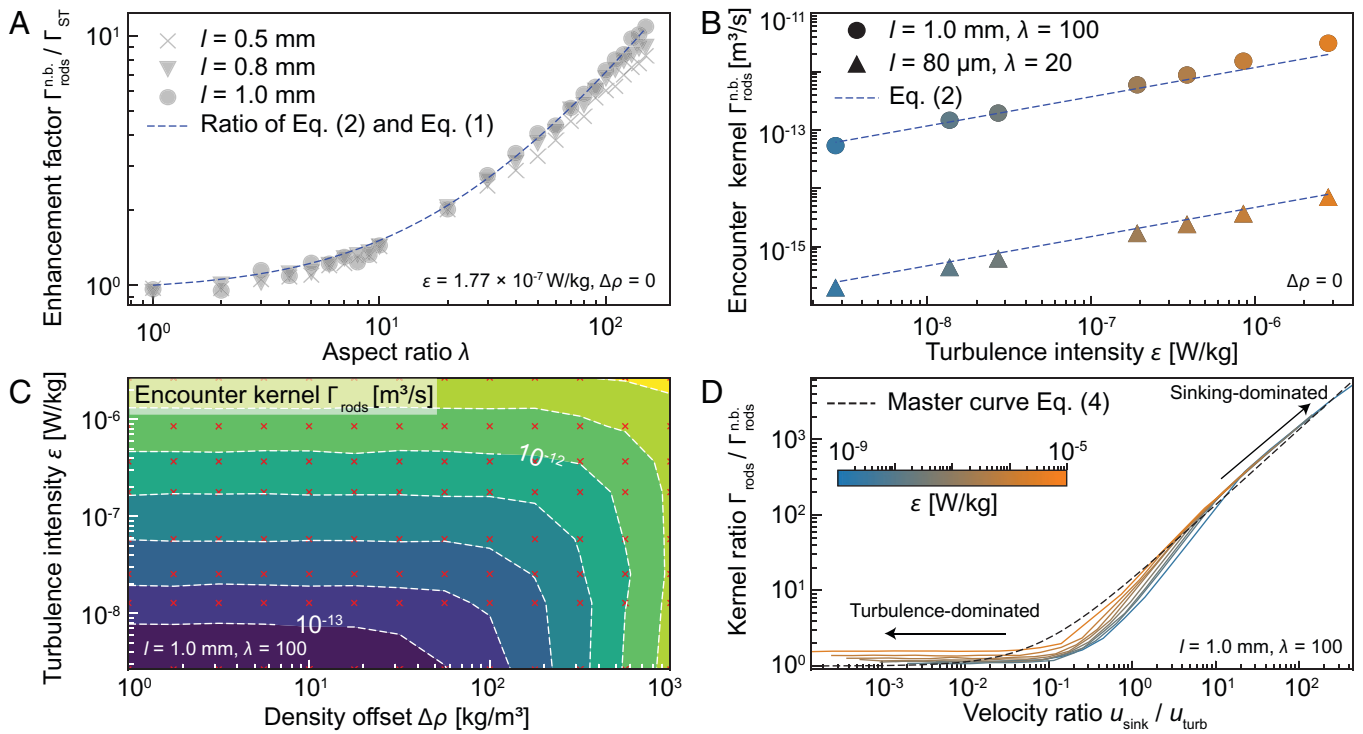


Fig. 2. Cell elongation enhances encounter rates between cells in turbulence. (A) The enhancement factor (kernel ratio) as a function of cell aspect ratio shows that elongation enhances encounter rates by up to an order of magnitude for neutrally buoyant cells compared to equal-volume spheres. We measured the encounter kernel for elongated, neutrally buoyant ($\Delta\rho = 0$) cells in numerical simulations (symbols) as a function of their aspect ratio λ , for three different cell lengths l and a given turbulence intensity ϵ . For each aspect ratio, we then normalized the kernel by the kernel for equal-volume spheres (Eq. 1). The blue dashed line represents the ratio $\Gamma_{rods}^{n.b.} / \Gamma_{ST}$ obtained by dividing Eq. 2 by Eq. 1 (SI Appendix). (B) Encounter kernel for two different elongated, neutrally buoyant phytoplankton cells as a function of turbulence intensity, computed from numerical simulations (symbols). Note the good agreement with the power law with exponent of 1/2 predicted by Eq. 2 (dashed line) and by dimensional analysis (SI Appendix). (C) Encounter kernel Γ_{rods} of elongated ($l = 1$ mm, $\lambda = 100$), sinking rods as a function of their density offset with surrounding water and of turbulence intensity. Red crosses denote data points from numerical simulations, used to obtain the contours and colormap by interpolation. (D) Master curve of the encounter rate of elongated phytoplankton. When rescaled by the encounter kernel for neutrally buoyant rods (Eq. 2), the simulated encounter kernels for buoyant rods (red crosses in C and additional data for heavier cells in SI Appendix, Fig. S1) collapse onto a single master curve (Eq. 4 and main text), for all values of density offset and turbulent intensity. The master curve shows a clear transition between a turbulence-dominated and a sinking-dominated regime.

between two cells sinking in a quiescent fluid or advected by turbulence, respectively. Rescaling the encounter kernel from our simulations (red crosses in Fig. 2C and additional data for heavier cells in SI Appendix, Fig. S1) by the neutrally buoyant kernel $\Gamma_{rods}^{n.b.}$ (Eq. 2) and plotting it against the velocity ratio u_{sink} / u_{turb} lead to an approximate collapse of the data (Fig. 2D), in good agreement with the master curve in Eq. 4 predicted by our hypothesis.

Eqs. 2 and 3 comprehensively quantify the encounter rate of elongated plankton in turbulence. Previous work on nonspherical objects in turbulence focused, for example, on preferential accumulations of elongated phytoplankton in turbulence (15), but did not address the role of elongation on encounters. Similarly, recent computations of collisions of ice crystals in clouds (30, 31) do not apply to the often highly elongated phytoplankton because they focused on spheroids with smaller aspect ratios, and because ice crystals are subject to inertial effects, which are not accessible to phytoplankton cells [characterized by fast relaxation timescales (15)] (Materials and Methods). We found that, for environmentally realistic conditions, encounter rates of elongated cells in turbulence are higher than those of spherical cells of equal volume [for comparison with cylinders in simple shear flow (32) see SI Appendix]. Because encounter rates are a foundation of many ecological processes (7), this finding has direct implications in how we understand and model these processes, as we demonstrate next by focusing on bloom clearance driven by marine snow formation and colony formation by elongated phytoplankton.

The enhanced encounter rates of elongated cells may be important in accelerating bloom clearance and the associated formation of marine snow (Fig. 3). Faster formation of marine snow may in turn increase the efficiency of the biological pump that transports primary production to depth because aggregates sink up to two orders of magnitude faster than individual cells (16), which reduces the fraction of organic carbon that is recycled in the upper photic zone (16, 33). To investigate bloom clearance driven by marine snow formation, we used our results to directly quantify the role of elongation in marine snow formation.

We considered a monospecific bloom of identical elongated phytoplankton, for example cell chains that reach a high concentration C_0 and, once they become senescent or die, start sinking and stick to each other upon encounter, forming marine snow. Cell stickiness can be triggered by both biotic and abiotic factors, including viral infection (34), nutrient limitation, and light stress (35). Here, we assume ideal stickiness, whereby every encounter between chains leads to chains sticking to each other. We then quantified the timescale of bloom clearance, associated with the conversion of biomass into marine snow, by computing a characteristic clearance timescale, T_c , as the time over which encounters convert half of the suspended chains into particles composed of two or more chains. This clearance timescale also represents the typical encounter time between individual chains, since this latter timescale is the bottleneck of the aggregation process, and subsequent encounters with additional chains (as well as with detritus and fecal pellets) occur much more rapidly (36). We

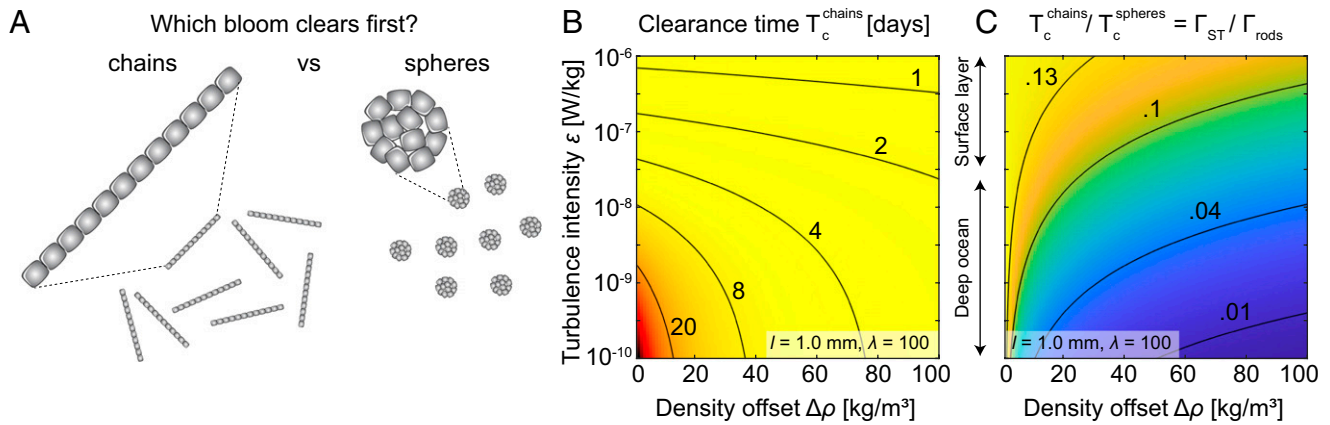


Fig. 3. Elongation of many phytoplankton cells or chains of cells accelerates bloom clearance through marine snow formation. (A) Which monospecific bloom clears first: one formed by chains of cells or by spheres of cells? (B) Predicted bloom clearance time T_c for highly elongated chains (e.g., *Trichodesmium*) for a broad range of ecologically relevant turbulence intensities and density offsets (chain concentration $C_0 = 10 \text{ mL}^{-1}$). (C) The ratio of the clearance time for chains and spheres (of equal volume) shows that marine snow forms at least sevenfold faster from chains than from spherical cells.

contrast the clearance time for identical chains with a hypothetical spherical cell arrangement with the same number of cells per particle (Fig. 3A) [for alternative characterization using critical concentrations (28) see *SI Appendix*]. The clearance time T_c is obtained by solving a simplified version of the Smoluchowski equation (*SI Appendix*)

$$T_c = (C_0\Gamma)^{-1}, \quad [5]$$

where Γ is the relevant encounter kernel. For example, for neutrally buoyant chains and spheres, from Eqs. 1 and 2 we have $T_c^{\text{chains}} = (C_0\Gamma_{\text{rods}}^{\text{n.b.}})^{-1}$ and $T_c^{\text{spheres}} = (C_0\Gamma_{\text{ST}})^{-1}$. The clearance time ratio $T_c^{\text{chains}}/T_c^{\text{spheres}} = \Gamma_{\text{ST}}/\Gamma_{\text{rods}}^{\text{n.b.}}$ is proportional to the inverse of the kernel ratio and our results thus predict that it is always lower for chains than for spheres (Fig. 2A), irrespective of the concentration C_0 . This difference is further magnified by the fact that dead or senescent phytoplankton at the end of a phytoplankton bloom tend to be negatively buoyant and sink, which further increases encounters between elongated cells (Eq. 3) but not between spherical cells (because identical spheres do not collide under gravitational settling) (13, 26). We now focus on two important examples of chain-forming cells, the globally distributed *Skeletonema* (37) and *Trichodesmium* (21).

Modeling negatively buoyant ($\Delta\rho = 50 \text{ kg/m}^3$) chain-forming diatom *Skeletonema* as chains consisting of 10 cells (29), each cell with dimensions $4 \times 8 \text{ }\mu\text{m}$ (3) (and thus $l = 80 \text{ }\mu\text{m}$, $\lambda = 20$ in our model), the clearance time is about 4 d for conditions representative of the ocean surface layer ($\varepsilon = 1 \times 10^{-6} \text{ W/kg}$) and chain concentration $C_0 = 500 \text{ mL}^{-1}$ (28). This short clearance timescale is consistent for example with the timescale of 1 wk needed to dissipate a recent bloom triggered by a volcano eruption in the North Pacific Ocean (38), which was dominated by *Skeletonema*. By contrast, the clearance time predicted for spheres of equal volume would have been more than 9 d. For the most elongated phytoplankton, such as the filaments of *Trichodesmium* [$l = 1 \text{ mm}$, $\lambda = 100$ (5, 6)] (*Movie S1*), the clearance times are even shorter and can be less than 2 d for a broad range of conditions and filament concentration $C_0 = 10 \text{ mL}^{-1}$ characteristic of high-density “slicks” (39–41) (Fig. 3B). As a result, the clearance time is seven to tens of times shorter for filaments than for equal-volume spheres (Fig. 3C). For example, for a turbulence intensity characteristic of the ocean surface layer ($\varepsilon = 1 \times 10^{-6} \text{ W/kg}$) (44) and an initial filament concentration of 1 mL^{-1} (45), colonies start to emerge in less than 1 wk, nearly nine times faster than they would if cells were spherical. Whether elongation in phytoplankton is a specific adaptation for colony formation remains unclear. Also, while our work highlights the importance of encounters in driving colony formation, the latter can also occur through growth, i.e., the replication of cells that do not separate. The relative importance of encounters vs. growth in driving colony formation in the natural environment remains an open question. However, our results highlight that elongation can substantially accelerate encounters and should thus be taken into account in evaluating the importance of colony formation via encounters vs. via growth.

Caledonian lagoon in less than 24 h (41) (although other clearance mechanisms cannot be ruled out, such as advection by currents or zooplankton grazing). By contrast, the clearance timescale of about 6 d predicted based on equal-volume spheres is substantially too high to explain this observation.

The enhanced encounter rates of elongated cells may also help to rationalize marine snow composition. Genera commonly found on diatom aggregates, a type of marine snow that forms following phytoplankton blooms, are *Nitzschia*, *Chaetoceros*, *Rhizosolenia*, *Leptocylindricus*, *Skeletonema*, and *Thalassionema* (19)—all of which either have elongated cells or grow as chains of cells. While this predominance may also reflect the relative prevalence of elongated species in the water column, our results suggest that an important role could be played by significantly enhanced encounter and thus coagulation rates among elongated species.

Our results also contribute to understanding colony formation among certain species of highly elongated phytoplankton. The needle-like cells of *Rhizosolenia* (λ up to 100) (3) or chains of cells of *Trichodesmium* (λ can exceed 100) (5, 6) often form colonies composed of large numbers of individuals, called mats (20) or tufts and puffs (21), which can have very different properties from the individuals, for example higher vertical migration speeds (42), different microbiomes (43), and different biogeochemical functions (20). Our results suggest that cell elongation facilitates the formation of such colonies by accelerating the rate at which they form from a suspension of individuals. For example, modeling *Trichodesmium* filaments as elongated rods ($l = 1 \text{ mm}$, $\lambda = 100$, $\Delta\rho = 80 \text{ kg/m}^3$) (5, 6, 42), our results suggest that for a turbulent intensity characteristic of the ocean surface layer ($\varepsilon = 1 \times 10^{-6} \text{ W/kg}$) (44) and an initial filament concentration of 1 mL^{-1} (45), colonies start to emerge in less than 1 wk, nearly nine times faster than they would if cells were spherical. Whether elongation in phytoplankton is a specific adaptation for colony formation remains unclear. Also, while our work highlights the importance of encounters in driving colony formation, the latter can also occur through growth, i.e., the replication of cells that do not separate. The relative importance of encounters vs. growth in driving colony formation in the natural environment remains an open question. However, our results highlight that elongation can substantially accelerate encounters and should thus be taken into account in evaluating the importance of colony formation via encounters vs. via growth.

Our work points to several potential extensions and to the need for experimental observations of specific microscale processes. We have assumed ideal cell stickiness, whereby every encounter results

in sticking. This was motivated by the fact that cells often become sticky as they become senescent or die (34, 35, 46). Stickiness values of less than 100% are straightforward to incorporate in our calculations (36) and would result in proportionally longer clearance times (e.g., a 50% stickiness would double the clearance time). However, the relative difference in the encounter timescale between elongated and spherical cells will remain unchanged, provided that stickiness is the same for both morphologies. Still, the dependence of stickiness on cell shape, as well as on hydrodynamic interactions (47, 48), remains an open question and will be affected by the mechanisms by which cells stick, a subject that will benefit from further experimental work. Finally, indirect support for our findings comes from observed adhesion rates of elongated cells or chains of *Skeletonema* and *Rhizosolenia* (28, 49). Those observed adhesion rates, when divided by encounter rates computed based on the spherical cell assumption, yielded stickiness values greater than 1 (i.e., around 2 to 4) (28, 49). As has already been recognized (28), such values of stickiness greater than 1 are physically unrealistic because it would mean that more adhesion events than encounter events occur. These observations then strongly point at encounter rates being higher than estimated based on the spherical cell assumption (28), a conclusion that is in line with our results on increased encounter rates due to cell elongation.

As for the environmental conditions investigated in our study, we restricted computations to moderate turbulence levels ($\varepsilon \leq 10^{-6}$ W/kg) (44), yet the encounter kernel we derived (Eq. 3) is also valid for higher levels of turbulence, as long as cells or chains are smaller than the Kolmogorov scale. For example, for a stronger turbulence intensity of $\varepsilon = 10^{-5}$ W/kg, the predicted clearance times for *Skeletonema* and *Trichodesmium* are about three times smaller than the values computed above for $\varepsilon = 1 \times 10^{-6}$ W/kg. Finally, we focused here on prolate cells in turbulence, and more work is needed to compute encounter kernels for oblate cells, such as *Coscinodiscus*. By extrapolating previous work on oblate cylinders in simple shear flow (32) to the case of turbulent flow, we estimate that thin *Coscinodiscus* cells (aspect ratio $\lambda = 0.1$) (3) will encounter each other in turbulence approximately twice as frequently as equal-volume spheres (independently of the turbulence intensity) (SI Appendix). This suggests that not only prolate phytoplankton, but oblate phytoplankton too, result in higher encounter rates than those expected based on the assumption of sphericity, providing motivation for further investigating encounter rates for the full range of cell morphologies.

In conclusion, we presented results from direct numerical simulations of plankton encounters in turbulence, taking into account elongation, and distilled these into a single master curve that illustrates how turbulence and sinking each contribute to encounters. We found that elongation can accelerate encounters, and thus decreases the timescale of the many ecological processes dependent on encounters, by up to an order of magnitude for neutrally buoyant cells and even more for buoyant ones, compared to spherical cells. Because to date most modeling of plankton encounters has assumed spherical cells (14), and because a majority of phytoplankton in the ocean are elongated (4), often with high aspect ratios (3), our results provide a substantial departure from the current understanding of ecological processes that depend on encounters. We illustrated the impact of accelerated encounters on bloom clearance and the associated process of marine snow formation, yet we expect that our results will be relevant for a range of other ecological processes, including mating (12), colony formation (20, 21), and biodiversification (3). Taken together, our work shows that the elongated shape of many phytoplankton species has far-reaching, hitherto neglected consequences on their ecology by exerting a fundamental control on encounter rates.

Materials and Methods

Turbulence Simulations. We perform fully resolved direct numerical simulations of the incompressible Navier-Stokes equations in the vorticity formulation with our code TurTLE. This fluid flow solver is a highly parallelized pseudospectral code that allows for the integration of particle species advected with the fluid flow (50). The incompressible Navier-Stokes equations take the form

$$\frac{\partial \mathbf{u}}{\partial t} + \mathbf{u} \cdot \nabla \mathbf{u} = -\nabla p + \nu \nabla^2 \mathbf{u} + \mathbf{f}, \quad [6a]$$

$$\nabla \cdot \mathbf{u} = 0. \quad [6b]$$

Here, \mathbf{u} is the three-dimensional velocity field, p denotes the kinematic pressure, and ν is the kinematic viscosity in code units. \mathbf{f} is a large-scale forcing that drives the flow to ensure a statistically stationary state.

We rescale the simulation units and parameters to physically and biologically relevant ones. In our simulations, we keep the large-scale forcing constant and adjust viscosity (and simulation resolution) to achieve ε in the range 10^{-9} to 10^{-6} W/kg, which corresponds to oceanic values up to moderate turbulence levels (44).

To convert from code units to physical units, let us denote ℓ and τ as the conversion factors from code units to physical units for space and time, respectively. Additionally, consider the integral length scale of the flow based on the longitudinal velocity autocorrelation function as L_{int} and the code integral length \tilde{L}_{int} . Following this convention, symbols with a tilde refer to code units whereas symbols without a tilde refer to physical units. Consistent with experiments in turbulence tanks, we set the integral length scale to $L_{\text{int}} = 10$ cm—since the simulation domain is a cube with size $\approx 6L_{\text{int}}$, our simulations represent a turbulence tank of about 200 to 300 L (51). From this we can fix ℓ as

$$L_{\text{int}} = \tilde{L}_{\text{int}} \ell \Rightarrow \ell = \frac{L_{\text{int}}}{\tilde{L}_{\text{int}}}. \quad [7]$$

Additionally, we have to match water viscosity to physical units, which fixes τ :

$$\nu = \tilde{\nu} \ell^2 \tau^{-1} \Rightarrow \tau = \frac{\tilde{\nu}}{\nu} \left(\frac{L_{\text{int}}}{\tilde{L}_{\text{int}}} \right)^2. \quad [8]$$

Using these conversion factors we can calculate the dissipation rate in physical units for a given dissipation rate in code units:

$$\varepsilon = \tilde{\varepsilon} \ell^2 \tau^{-3}. \quad [9]$$

Finally, we set the rod length to a fixed length in physical units, i.e., millimeters, and rescale it correspondingly into code units. In Fig. 2A, we explored three rod lengths in the neutrally buoyant case, 0.5, 0.8, and 1.0 mm. In Fig. 2B, we studied also neutrally buoyant rods and varied both aspect ratio and rod length, covering the cases $\lambda = 100$ and $l = 1.0$ mm, as well as $\lambda = 20$ and $l = 80$ μm . Finally, in Fig. 2C and D we kept the aspect ratio $\lambda = 100$ and length $l = 1.0$ mm fixed and scanned the density offset variable $\Delta\rho$ and the turbulence intensity ε . In Fig. 2C, we concentrated on the biologically relevant $\Delta\rho$ regime, while the collapse in Fig. 2D is based on a larger dataset that includes heavier rods to resolve the sinking-dominated regime—this larger dataset is shown in SI Appendix, Fig. S1. Other relevant values used for the simulations are reported in SI Appendix, Table S1.

Simulation of Sinking Rods. The investigation of sinking anisotropic particles in turbulent flows has recently gained much attention, from a fundamental point of view, but also with respect to applications in the atmospheric sciences and marine ecology (15, 30, 31, 52–55).

To model sinking cells, we describe the positional and orientational dynamics of small thin elongated ellipsoidal particles sinking in a turbulent flow with no back reaction onto the flow, and we neglect inertial effects owing to the fast relaxation timescales of planktonic cells (15, 52). Specifically, the translational relaxation timescale τ_p for elongated particles is $\tau_p = \rho^2 \ln(\lambda + \sqrt{\lambda^2 - 1}) / (18\mu\lambda\sqrt{\lambda^2 - 1})$ (52), where ρ is the cell density, l and λ are the cell's length and aspect ratio, and μ is the fluid's dynamic viscosity. Even in the case of the rather large *Trichodesmium* filaments ($l = 1$ mm, $\lambda = 100$), assuming cell density $\rho = 1,000$ kg/m³ and water viscosity $\mu = 1$ m \cdot Pa \cdot s,

the translational relaxation time is $\tau_p = 3 \times 10^{-5}$ s, much lower than the Kolmogorov timescale of 1 s characterizing the strongest levels of turbulence studied here (with turbulence intensity $\varepsilon = 1 \times 10^{-6}$ W/kg). Even for the very high turbulence that can intermittently arise within meters below the ocean surface ($\varepsilon = 1 \times 10^{-4}$ W/kg), this relaxation timescale is about four orders of magnitude smaller than the corresponding Kolmogorov timescale of 0.1 s. Additionally, the rotational relaxation times are known to be even shorter than translational ones (56).

The particles are advected by the flow and have an orientation-dependent sinking velocity (57)

$$\dot{\mathbf{x}} = \mathbf{u} + u_s (\beta_0 \hat{\mathbf{g}} + \beta_1 \hat{\mathbf{p}} \cdot \hat{\mathbf{g}} \hat{\mathbf{p}}). \quad [10]$$

Here, \mathbf{x} is the position of the particle, \mathbf{u} is the velocity field governed by Eq. 6 at the position of the particle, $\hat{\mathbf{p}}$ is the particle orientation, and $\hat{\mathbf{g}}$ is the direction of the gravitational acceleration. The characteristic sinking speed of a single particle is given by

$$u_s = \frac{\Delta \rho V_{\text{rod}} g}{8\pi \mu l}. \quad [11]$$

Here, $\Delta \rho := \rho_p - \rho_f$ is the offset between the particle ρ_p and the fluid ρ_f density, g is the magnitude of the gravitational acceleration, μ is the dynamic viscosity of the fluid, and the length of the rods is given by l . Eq. 10 was derived for ellipsoidal particles. However, for consistency with our numerical collision algorithm (see below) we use here the volume of rods with spherical caps $V_{\text{rod}} = \pi l^3 / (4\lambda^2) (1 - 1/3\lambda)$ with the same aspect ratio λ . Finally, β_0 and β_1 are functions that depend on λ and are given by (57)

$$\beta_0(\lambda) = \frac{\lambda^2}{\lambda^2 - 1} + \frac{2\lambda^3 - 3\lambda}{(\lambda^2 - 1)^{3/2}} \ln \left[\lambda + (\lambda^2 - 1)^{1/2} \right] \quad [12a]$$

$$\beta_1(\lambda) = \frac{-3\lambda^2}{\lambda^2 - 1} + \frac{2\lambda}{(\lambda^2 - 1)^{3/2}} \ln \left[\lambda + (\lambda^2 - 1)^{1/2} \right] + \frac{\lambda - 2\lambda^3}{(\lambda^2 - 1)^{3/2}} \ln \left[\lambda - (\lambda^2 - 1)^{1/2} \right]. \quad [12b]$$

To determine the particles' orientational dynamics, we approximate their shape as ellipsoids with aspect ratio λ and integrate the particle orientation vector using Jeffery's equations (58)

$$\dot{\hat{\mathbf{p}}} = \frac{1}{2} \boldsymbol{\omega} \times \hat{\mathbf{p}} + \frac{\lambda^2 - 1}{\lambda^2 + 1} (\mathbf{S}\hat{\mathbf{p}} - \hat{\mathbf{p}}\hat{\mathbf{p}}^T\mathbf{S}\hat{\mathbf{p}}). \quad [13]$$

Here, $\boldsymbol{\omega} = \nabla \times \mathbf{u}$ is the vorticity, and $S_{ij} = (\partial_i u_j + \partial_j u_i) / 2$ is the strain tensor, both of which induce particle spinning and tumbling depending on the shape of the particles.

Encounter Detection Algorithm. Particle encounters are measured using the so-called ghost encounters (59); i.e., particles may overlap but do not interact during collisions. For the encounter detection algorithm, we approximate the particles as thin rods with spherical caps (Fig. 1D). Encounters between thin rods can be calculated by searching for the minimal distance between the two symmetry axes of the rods. Consider a first rod at a position \mathbf{x} with orientation $\hat{\mathbf{p}}$ and a second rod with orientation $\hat{\mathbf{q}}$ at a position \mathbf{y} . Both rods have length l and width w . Positions along the rods may be parameterized by use of the parameters $t, s \in [-1, 1]$, such that any point along the symmetry axis of the rods may be written as

$$\mathbf{r}_1(t) = \mathbf{x} + t \left(1 - \frac{1}{\lambda} \right) \frac{l}{2} \hat{\mathbf{p}}; \quad t \in [-1, 1] \quad [14]$$

for the first rod and

$$\mathbf{r}_2(s) = \mathbf{y} + s \left(1 - \frac{1}{\lambda} \right) \frac{l}{2} \hat{\mathbf{q}}; \quad s \in [-1, 1] \quad [15]$$

for the second rod. The distance between two points on the symmetry axis of the rods is then

$$\begin{aligned} \text{dist}(t, s) &= \sqrt{|\mathbf{r}_1(t) - \mathbf{r}_2(s)|^2} \\ &= \sqrt{\left[\frac{l}{2} \left(1 - \frac{1}{\lambda} \right) (\hat{\mathbf{p}}t - \hat{\mathbf{q}}s) + \Delta \mathbf{x} \right]^2}, \quad [16] \end{aligned}$$

where $\Delta \mathbf{x} = \mathbf{x} - \mathbf{y}$. The minimum distance can be found by setting the gradient of this distance function to zero. This leads to a linear system, which can be solved leading to

$$\begin{pmatrix} t_{\min} \\ s_{\min} \end{pmatrix} = \frac{2}{l(\lambda - 1)} \frac{\lambda}{(\hat{\mathbf{p}} \cdot \hat{\mathbf{q}})^2 - 1} \times \begin{pmatrix} 1 & -\hat{\mathbf{p}} \cdot \hat{\mathbf{q}} \\ \hat{\mathbf{p}} \cdot \hat{\mathbf{q}} & -1 \end{pmatrix} \begin{pmatrix} \Delta \mathbf{x} \cdot \hat{\mathbf{p}} \\ \Delta \mathbf{x} \cdot \hat{\mathbf{q}} \end{pmatrix}. \quad [17]$$

This yields the minimum distance if $|t_{\min}| \leq 1$ and $|s_{\min}| \leq 1$. If $|t_{\min}| \geq 1$ or $|s_{\min}| \geq 1$, we must search for the minimum distance along $|t| = 1$ and $|s| = 1$. In these latter cases, the minimum distance can be analytically found. For $t_{\min} = \pm 1$

$$s_{\min} = t_{\min} \hat{\mathbf{p}} \cdot \hat{\mathbf{q}} + \frac{2}{l} \frac{\lambda}{\lambda - 1} \Delta \mathbf{x} \cdot \hat{\mathbf{q}}. \quad [18]$$

For $s_{\min} = \pm 1$

$$t_{\min} = s_{\min} \hat{\mathbf{p}} \cdot \hat{\mathbf{q}} - \frac{2}{l} \frac{\lambda}{\lambda - 1} \Delta \mathbf{x} \cdot \hat{\mathbf{p}}. \quad [19]$$

Particle overlaps at a given time snapshot can then be detected by $\text{dist}(t_{\min}, s_{\min}) < w$. This means, at their minimum distance, the rods are less than one width apart from one another.

We then keep track of overlaps of particle pairs. At every time step we compare the overlap of particle pairs with the ones from the previous time step. If the overlap of a particle pair is detected that was not detected in the previous time step, we count that overlap change as a new encounter. This new encounter contributes to the total number of new encounters N_{enc} . Given a number of new encounters N_{enc} in a given time T , volume V , and total number of particles N_{part} , the encounter kernel is then obtained as (59)

$$\Gamma = \frac{2V N_{\text{enc}}}{N_{\text{part}}^2 T}. \quad [20]$$

In our simulations, the simulation domain is a cube with side length 2π and volume $V = 8\pi^3$ in code units. We typically run the simulations for time T on the order of several integral timescales (defined as $L_{\text{int}}/u_{\text{rms}}$). For our choice of particle numbers N_{part} (SI Appendix, Table S1), these simulation times guarantee statistical convergence of the kernel estimate in Eq. 20. We also remove an initial transient time of two integral timescales, which allows for the spatial and orientational distributions of particles to reach a statistically stationary state. Thus, with the number of detected encounters (N_{enc} is on the order of 1,000 encounters per integral timescale), Eq. 20 gives us an encounter kernel in code units, with units of $\text{space}^3/\text{time}$. Finally, using the transformation factors in Eqs. 7 and 8 this quantity may then be transformed into physical units.

Data Availability. The code for the turbulence simulations data has been deposited in a publicly accessible repository (<https://gitlab.mpcdf.mpg.de/TurtLE/turtle>) and is described in (50). The relevant study data is displayed in the manuscript and the SI Appendix.

ACKNOWLEDGMENTS. We thank Lukas Bentkamp and Ewelina Borowiecka for help with the figures, and Ulrike Pfreundt, Karen Grace Bondoc-Naumovitz, and Kay Bidle for discussions. We thank Bérenger Bramas for code development related to the particle tracking and collision functionality in TurTLE. Fig. 3 was partly generated using Servier Medical Art, provided by Servier, licensed under a Creative Commons Attribution 3.0 unported license. We gratefully acknowledge funding from an ETH Zurich Postdoctoral Fellowship and Swiss National Science Foundation Ambizione Grant PZ00P2_202188 (to J.S.); from a Gordon and Betty Moore Foundation Symbiosis in Aquatic Systems Investigator Award (GBMF9197), from the Simons Foundation through the Principles of Microbial Ecosystems collaboration (Grant 542395), from the Swiss National Science Foundation (205321_207488), and from the Swiss National Science Foundation, National Centre of Competence in Research Microbiomes (51NF40 180575) (to R.S.); and from a Fulbright-Cottrell Award grant and the Max Planck Society (to M.W.).

Author affiliations: ^aMax Planck Institute for Dynamics and Self-Organization, 37077 Göttingen, Germany; ^bInstitute of Environmental Engineering, Department of Civil, Environmental and Geomatic Engineering, ETH Zurich, 8093 Zurich, Switzerland; ^cHPC Application Support, Max Planck Computing and Data Facility, 85748 Garching, Germany; and ^dTheoretical Physics I, University of Bayreuth, 95440 Bayreuth, Germany

1. P. G. Falkowski, The role of phytoplankton photosynthesis in global biogeochemical cycles. *Photosynth. Res.* **39**, 235–258 (1994).
2. P. G. Falkowski, R. T. Barber, V. Smetacek, Biogeochemical controls and feedbacks on ocean primary production. *Science* **281**, 200–207 (1998).
3. A. Ryabov *et al.*, Shape matters: The relationship between cell geometry and diversity in phytoplankton. *Ecol. Lett.* **24**, 847–861 (2021).
4. W. R. Calvano, E. Boss, L. Karp-Boss, Inherent optical properties of non-spherical marine-like particles—from theory to observation. *Oceanogr. Mar. Biol. Annu. Rev.* **45**, 1–38 (2007).
5. R. M. Letelier, D. Karl, Role of Trichodesmium spp. in the productivity of the subtropical North Pacific Ocean. *Mar. Ecol. Prog. Ser.* **133**, 263–273 (1996).
6. A. E. White, K. S. Watkins-Brandt, M. J. Church, Temporal variability of Trichodesmium spp. and diatom-diazotroph assemblages in the North Pacific subtropical gyre. *Front. Mar. Sci.* **5**, 27 (2018).
7. T. Kiorboe, *A Mechanistic Approach to Plankton Ecology* (Princeton University Press, 2008).
8. K. W. Wirtz, Non-uniform scaling in phytoplankton growth rate due to intracellular light and CO₂ decline. *J. Plankton Res.* **33**, 1325–1341 (2011).
9. M. Pančić, T. Kiorboe, Phytoplankton defence mechanisms: Traits and trade-offs. *Biol. Rev. Camb. Philos. Soc.* **93**, 1269–1303 (2018).
10. A. Sengupta, F. Carrara, R. Stocker, Phytoplankton can actively diversify their migration strategy in response to turbulent cues. *Nature* **543**, 555–558 (2017).
11. L. Naselli-Flores, R. Barone, Invited review—fight on plankton! Or, phytoplankton shape and size as adaptive tools to get ahead in the struggle for life. *Cryptogam., Algal.* **32**, 157–204 (2011).
12. J. S. Font-Muñoz *et al.*, Collective sinking promotes selective cell pairing in planktonic pennate diatoms. *Proc. Natl. Acad. Sci. U.S.A.* **116**, 15997–16002 (2019).
13. J. Słomka, R. Stocker, On the collision of rods in a quiescent fluid. *Proc. Natl. Acad. Sci. U.S.A.* **117**, 3372–3374 (2020).
14. A. B. Burd, G. A. Jackson, Particle aggregation. *Annu. Rev. Mar. Sci.* **1**, 65–90 (2009).
15. M. N. Ardekani *et al.*, Sedimentation of inertia-less prolate spheroids in homogenous isotropic turbulence with application to non-motile phytoplankton. *J. Fluid Mech.* **831**, 655–674 (2017).
16. A. L. Alldredge, C. C. Gotschalk, Direct observations of the mass flocculation of diatom blooms: Characteristics, settling velocities and formation of diatom aggregates. *Deep. Sea Res.* **A36**, 159–171 (1989).
17. P. W. Boyd, H. Claustre, M. Levy, D. A. Siegel, T. Weber, Multi-faceted particle pumps drive carbon sequestration in the ocean. *Nature* **568**, 327–335 (2019).
18. U. Alcolombri *et al.*, Sinking enhances the degradation of organic particles by marine bacteria. *Nat. Geosci.* **14**, 775–780 (2021).
19. D. Thornton, Diatom aggregation in the sea: Mechanisms and ecological implications. *Eur. J. Phycol.* **37**, 149–161 (2002).
20. T. A. Villareal, M. A. Altabet, K. Culver-Rymsza, Nitrogen transport by vertically migrating diatom mats in the North Pacific Ocean. *Nature* **363**, 709–712 (1993).
21. D. G. Capone, J. P. Zehr, H. W. Paerl, B. Bergman, E. J. Carpenter, Trichodesmium, a globally significant marine cyanobacterium. *Science* **276**, 1221–1229 (1997).
22. J. P. Zehr, D. G. Capone, Changing perspectives in marine nitrogen fixation. *Science* **368**, eaay9514 (2020).
23. T. A. Villareal, E. J. Carpenter, Buoyancy regulation and the potential for vertical migration in the oceanic cyanobacterium trichodesmium. *Microb. Ecol.* **45**, 1–10 (2003).
24. A. E. Walsby, The properties and buoyancy-providing role of gas vacuoles in Trichodesmium Ehrenberg. *Br. Phycol. J.* **13**, 103–116 (1978).
25. P. G. F. Saffman, J. S. Turner, On the collision of drops in turbulent clouds. *J. Fluid Mech.* **1**, 16–30 (1956).
26. G. Falkovich, A. Fouxon, M. G. Stepanov, Acceleration of rain initiation by cloud turbulence. *Nature* **419**, 151–154 (2002).
27. J. M. C. Hutchinson, P. M. Waser, Use, misuse and extensions of “ideal gas” models of animal encounter. *Biol. Rev. Camb. Philos. Soc.* **82**, 335–359 (2007).
28. T. Kiorboe, C. Lundsgaard, M. Olesen, J. L. S. Hansen, Aggregation and sedimentation processes during a spring phytoplankton bloom: A field experiment to test coagulation theory. *J. Mar. Res.* **52**, 297–323 (1994).
29. M. Takabayashi *et al.*, The effect of nutrient availability and temperature on chain length of the diatom, *Skeletonema costatum*. *J. Plankton Res.* **28**, 831–840 (2006).
30. C. Siewert, R. Kunnen, W. Schröder, Collision rates of small ellipsoids settling in turbulence. *J. Fluid Mech.* **758**, 686–701 (2014).
31. J. Jucha, A. Naso, E. Lévêque, A. Pumir, Settling and collision between small ice crystals in turbulent flows. *Phys. Rev. Fluids* **3**, 014604 (2018).
32. V. Singh, D. L. Koch, A. D. Stroock, Ideal rate of collision of cylinders in simple shear flow. *Langmuir* **27**, 11813–11823 (2011).
33. E. Bar-Zeev, I. Avishay, K. D. Bidle, I. Berman-Frank, Programmed cell death in the marine cyanobacterium Trichodesmium mediates carbon and nitrogen export. *ISME J.* **7**, 2340–2348 (2013).
34. C. P. Laber *et al.*, Coccolithovirus facilitation of carbon export in the North Atlantic. *Nat. Microbiol.* **3**, 537–547 (2018).
35. I. Berman-Frank, G. Rosenberg, O. Levitan, L. Haramaty, X. Mari, Coupling between autocatalytic cell death and transparent exopolymeric particle production in the marine cyanobacterium Trichodesmium. *Environ. Microbiol.* **9**, 1415–1422 (2007).
36. G. A. Jackson, A model of the formation of marine algal flocs by physical coagulation processes. *Deep. Sea Res.* **A37**, 1197–1211 (1990).
37. W. H. C. F. Kooistra *et al.*, Global diversity and biogeography of *Skeletonema* species (bacillariophyta). *Protist* **159**, 177–193 (2008).
38. S. T. Wilson *et al.*, Kilauea lava fuels phytoplankton bloom in the North Pacific Ocean. *Science* **365**, 1040–1044 (2019).
39. W. M. Dunstan, J. Hoford, The distribution of planktonic blue green algae related to the hydrography of the Georgia Bight. *Bull. Mar. Sci.* **27**, 824–829 (1977).
40. M. Rodier, R. Le Borgne, Population and trophic dynamics of Trichodesmium thiebautii in the SE lagoon of New Caledonia. Comparison with *T. erythraeum* in the SW lagoon. *Mar. Pollut. Bull.* **61**, 349–359 (2010).
41. D. Spungin *et al.*, Mechanisms of Trichodesmium demise within the New Caledonian lagoon during the VAHINE mesocosm experiment. *Biogeosciences* **13**, 4187–4203 (2016).
42. A. E. White, Y. H. Spitz, R. M. Letelier, Modeling carbohydrate ballasting by Trichodesmium spp. *Mar. Ecol. Prog. Ser.* **323**, 35–45 (2006).
43. M. Rouco, S. T. Haley, S. T. Dyhrman, Microbial diversity within the Trichodesmium holobiont. *Environ. Microbiol.* **18**, 5151–5160 (2016).
44. P. J. S. Franks, B. G. Inman, J. A. MacKinnon, M. H. Alford, A. F. Waterhouse, Oceanic turbulence from a planktonic perspective. *Limnol. Oceanogr.* **67**, 348–363 (2021).
45. E. J. Carpenter, A. Subramanian, D. G. Capone, Biomass and primary productivity of the cyanobacterium Trichodesmium spp. in the tropical N Atlantic Ocean. *Deep Sea Res. 1 Ocean. Res. Pap.* **51**, 173–203 (2004).
46. T. Kiorboe, J. L. S. Hansen, Phytoplankton aggregate formation: Observations of patterns and mechanisms of cell sticking and the significance of exopolymeric material. *J. Plankton Res.* **15**, 993–1018 (1993).
47. D. L. Koch, E. S. G. Shaqfeh, The instability of a dispersion of sedimenting spheroids. *J. Fluid Mech.* **209**, 521–542 (1989).
48. V. Botte, M. R. D’Alcalá, M. Montresor, Hydrodynamic interactions at low Reynolds number: An overlooked mechanism favouring diatom encounters. *J. Plankton Res.* **35**, 914–918 (2013).
49. A. Engel, The role of transparent exopolymer particles (TEP) in the increase in apparent particle stickiness (α) during the decline of a diatom bloom. *J. Plankton Res.* **22**, 485–497 (2000).
50. C. C. Lalescu, B. Bramas, M. Rampp, M. Wilczek, An efficient particle tracking algorithm for large-scale parallel pseudo-spectral simulations of turbulence. *Comput. Phys. Commun.* **278**, 108406 (2022).
51. Ó. Guadayol, F. Peters, J. E. Stiansen, C. Marrasé, A. Lohrmann, Evaluation of oscillating grids and orbital shakers as means to generate isotropic and homogeneous small-scale turbulence in laboratory enclosures commonly used in plankton studies. *Limnol. Oceanogr. Methods* **7**, 287–303 (2009).
52. G. A. Voth, A. Soldati, Anisotropic particles in turbulence. *Annu. Rev. Fluid Mech.* **49**, 249–276 (2017).
53. A. Naso, J. Jucha, E. Lévêque, A. Pumir, Collision rate of ice crystals with water droplets in turbulent flows. *J. Fluid Mech.* **845**, 615–641 (2018).
54. P. Anand, S. S. Ray, G. Subramanian, Orientation dynamics of sedimenting anisotropic particles in turbulence. *Phys. Rev. Lett.* **125**, 034501 (2020).
55. S. Brizzolara *et al.*, Fiber tracking velocimetry for two-point statistics of turbulence. *Phys. Rev. X* **11**, 031060 (2021).
56. C. Marchioli, L. Zhao, H. I. Andersson, On the relative rotational motion between rigid fibers and fluid in turbulent channel flow. *Phys. Fluids* **28**, 013301 (2016).
57. J. Happel, H. Brenner, *Low Reynolds Number Hydrodynamics: With Special Applications to Particulate Media* (Springer Science & Business Media, 2012), **vol. 1**.
58. G. B. Jeffery, L. N. H. Filon, The motion of ellipsoidal particles immersed in a viscous fluid. *Proc. R. Soc. Lond. A Contain. Pap. Math. Phys. Character* **102**, 161–179 (1922).
59. L. P. Wang, A. S. Wexler, Y. Zhou, On the collision rate of small particles in isotropic turbulence. I. Zero-inertia case. *Phys. Fluids* **10**, 266–276 (1998).